# LARADO: A Sensor for On-orbit Detection of Lethal Non-Trackable Debris

**Andrew C. Nicholas, Josh M. Wolf, Lee J. Kordella, Charles M. Brown, Ted T. Finne, Kenneth D. Marr, Scott A. Budzien, Ivan J. Galysh, Christoph R. Englert**
*U.S. Naval Research Laboratory, Washington, DC*

**ABSTRACT**

Objects in the size range of 0.1 mm to 3 cm are not currently trackable but have enough kinetic energy for lethal consequences to spacecraft. The detection of small orbital debris, both potentially posing a risk to most space missions, requires a combination of a large sensor area and large time coverage. For example, a sensor with a time area product of 3 $m^2$years is considered to be able to make a significant contribution to our understanding of the near-Earth small debris population. Deploying large sensors, however, is generally resource intensive, due to their size and weight. The light sheet concept, allows the creation of a "virtual witness plate", which is created without any supporting physical structure and therefore presents an attractive opportunity for the detection small debris anywhere between low Earth orbit to interplanetary space. Recent technology maturation efforts in the laboratory successfully detected small debris 1.6 mm moving at 6.58 km/s. NRL is building the NASA funded instrument as a technology maturation effort for a flight demonstration on STPSat-7 in 2024. In this presentation, we will describe the instrument, present the laboratory data and analysis, and describe the instrument details for the STPSat-7 spacecraft slated for launch via the DoD Space Test Program in Q1 CY2024.

## 1. INTRODUCTION

The number of man-made debris objects orbiting Earth [1], or orbital debris, as seen in Fig. 1, is increasing at an alarming rate, resulting in the increased probability of degradation, damage, or destruction of operating spacecraft. In particular, small objects (10cm to 1 μm) in Low Earth Orbit (LEO) are of concern because they are abundant, difficult to track or even to detect on a routine basis, and have enough kinetic energy to damage spacecraft [2,3]. Fragmentation debris has created three, as annotated in Fig. 1, recent step increases in the number of objects related to: 1) the 2007 Chinese ASAT test, 2) the 2009 Iridium/COSMOS collision, and 3) the 2021 Russian ASAT test. Objects in the size range of several cm down to 0.1 mm are too small to be tracked effectively but have enough kinetic energy to cause anomalies or catastrophic damage to spacecraft. Small objects moving at orbital velocities pack enough kinetic energy do serious damage as illustrated in Fig. 2. We call this category of debris "lethal non-trackable". Due to the increasing debris population, it is reasonable to assume that improved capabilities for on-orbit damage attribution, in addition to increased capabilities to detect and track small objects are needed. In this paper we present an instrument to detect debris in this lethal non-trackable category and to help characterize such debris distributions. The instrument layout and configuration on our host satellite, STPSat-7, will be described. STPSat-7 and its launch are provided by the DoD Space Test Program STPSat-7.

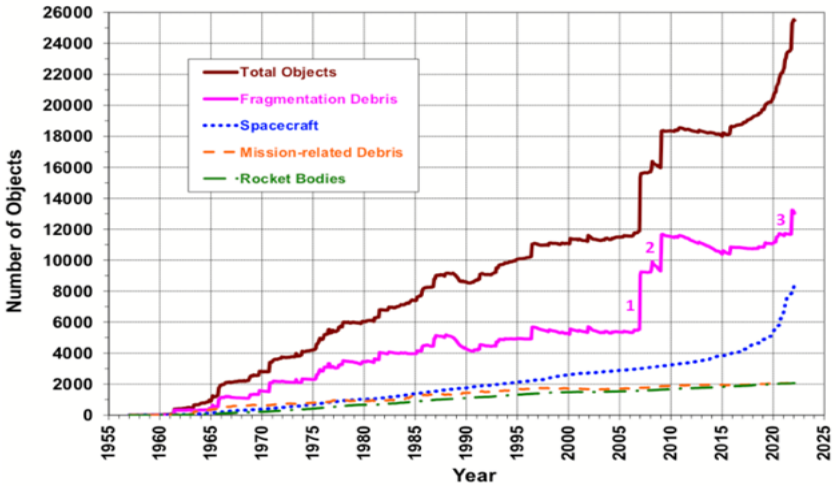


Fig. 1. Historical count of cataloged space objects.

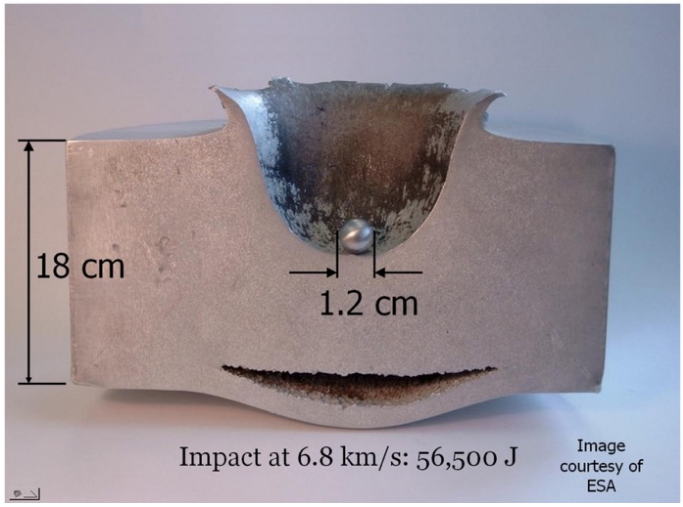


Fig. 2. Damage caused by a 1.2 cm diameter aluminum sphere striking an 18 cm thick plate of aluminum at 6.8 km/s. (Photo courtesy of ESA)

## 2. SENSOR CONCEPT

The LARADO sensor concept is based on creating a sheet of light in front of the host spacecraft and observing photons scattered by objects passing through the lightsheet. The lightsheet is created via a collimated light source that is connected to a diffusive optic, such as an axicon, Powell lens, or engineered diffuser. An optical lens coupled to a detector provides a method to monitor the scene. This system creates a virtual witness plate (VWP) for debris observations as seen in Fig. 3. The functional area of the virtual witness plate is scalable and defined by the components of the system: the power of the laser, the diffusive optic, the optics field of view (FOV) and aperture, and the detector sensitivity. The scalable nature of this instrument is unique in that it allows significant area coverage when compared with debris detection phenomenology that rely on impact observations. However, the data from these two methods are complementary as the impact method can also infer the mass density of the debris. A detailed description of the sensor concept and modeling is provided by Englert et al. [4] and Nicholas et al. [5], respectively. The DoD Space Test Program is developing the STPSat-7 spacecraft and mission that will host the LARADO sensor.

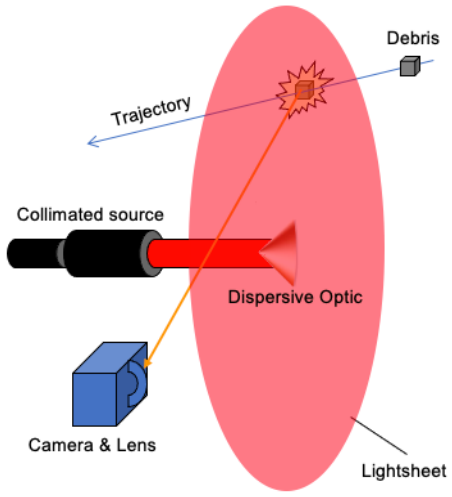


Fig. 3. Representative components for the LARADO sensor concept depicting the creation of the lightsheet, or virtual witness plate, and debris passing through it scattering photons to the optical detection system.

## 3. STPSat-7

STPSat-7 is a small ESPA class spacecraft with the LARADO instrument components mounted on the zenith panel. Due to limited bandwidth on STPSat-7, we are unable to downlink all of the raw images from the LARADO sensor,

therefore, we designed LARADO with two cameras that view the lightsheet from different vantage points. One camera views the lightsheet from an isometric perspective and one camera views parallel to the lightsheet. The parallel camera FOV can be reduced to only view the width of the lasersheet reducing the amount of on-board memory and processing power required for event detection. When an event is detected, it will trigger the spacecraft to download data from both camera views. This technique significantly reduced the amount of data telemetered to the ground, allows the parallel view camera to operate at a faster cadence, reduces the complexity of the on-board processing, and provides a second view to discriminate false positives that may appear in a single camera due to cosmic rays. The STPSat-7 LARADO configuration is presented in Fig. 4, the upper left panel showing the laser sheet (purple) mounted on the zenith face of the spacecraft near the ram side and the parallel camera FOV (blue). The lower left shows the parallel camera boresight view (dark blue) with the purple representing the laser sheet. The top right panel (ram direction is to the right) presents a view of the STPSat-7 starboard panel depicting the location of the zenith mounted isometric view camera and it's FOV (green). Area coverage of the lasersheet from each camera is depicted in Fig. 5 and provided in Tables 1 and 2.

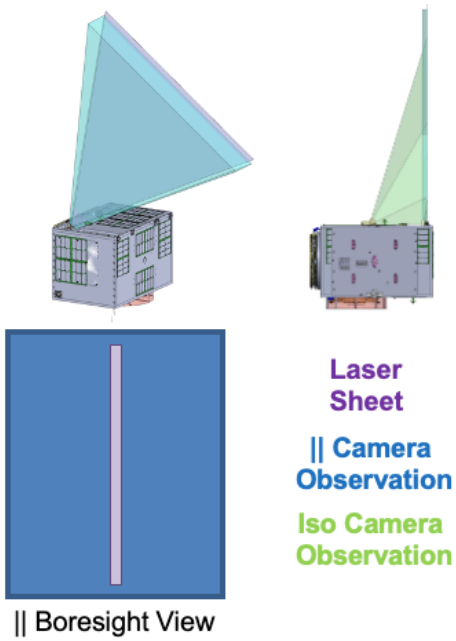


Fig. 4. Configuration of lightsheet (purple) isometric (green) and parallel (blue) viewing cameras on STPSat-7.

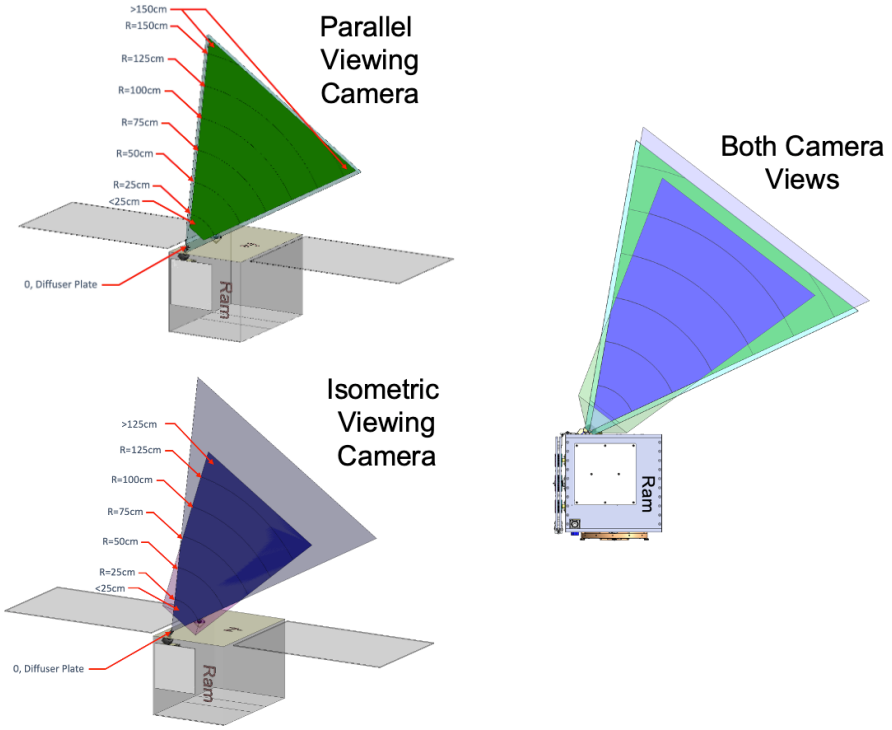


Fig. 5. Configuration of lightsheet (purple) isometric (green) and parallel (blue) viewing cameras on STPSat-7.

Table 1. Parallel View Area Coverage

| Radius (cm) | Sep (m) | Range/Radius (cm) | Area ($m^2$) | ∑ Area ($m^2$) |
|---|---|---|---|---|
| <25 | 0.1962 | <25 | 0.0226 | 0.0226 |
| 25 | 0.3174 | 25 - 50 | 0.0927 | 0.1153 |
| 50 | 0.5667 | 50 - 75 | 0.1527 | 0.268 |
| 75 | 0.8165 | 75 - 100 | 0.2127 | 0.4807 |
| 100 | 1.0663 | 100 -125 | 0.2727 | 0.7534 |
| 125 | 1.3163 | 125 - 150 | 0.2952 | 1.0486 |
| 150 | 1.5018 | >150 | 0.0317 | 1.0803 |

Table 2. Isometric View Area Coverage

| Radius (cm) | Sep (m) | Range/Radius (cm) | Area ($m^2$) | ∑ Area ($m^2$) |
|---|---|---|---|---|
| <25 | 0.4512 | <25 | 0.0254 | 0.0254 |
| 25 | 0.5114 | 25 - 50 | 0.0927 | 0.1181 |
| 50 | 0.6791 | 50 - 75 | 0.1513 | 0.2694 |
| 75 | 0.8865 | 75 - 100 | 0.1922 | 0.4616 |
| 100 | 1.1116 | 100 -125 | 0.2278 | 0.6894 |
| 125 | 1.3455 | >125 | 0.1448 | 0.8342 |
| >125 | 1.4476 | | | |

## 4. AVGR TESTING

### 4.1 Chamber

The Ames Vertical Gun Range (AVGR) [6] is NASA's premiere hypervelocity impact facility for Planetary Geology and Geophysics research. The AVGR was brought on-line in 1966 to develop a better understanding of lunar surface geomorphology in support of the Apollo program and has since provided critical data that helped enable a variety of NASA missions including: Cassini, Deep Impact, LCROSS, Mars Odyssey, Stardust, and MER (Mars Exploration Rovers). With its unique hinged gun apparatus, the AVGR can vary the impact angle relative to the gravity vector (from horizontal to vertical). Targets are contained within a large impact chamber, as seen in Fig. 6, that can be evacuated to simulate impacts on an airless body or backfilled with air or various gases to simulate different environments. Typical impactors range in size from 1/16" to 1/4" (1.5875 to 6.35mm) in diameter, are of various composition (metal, plastic, glass, ceramic, mineral, etc.), and can be launched to speeds ranging from 0.5 to 7 km/s. A robust suite of high-speed video cameras (Vision Research and Shimadzu), lenses and lighting options can be positioned at many impact chamber window ports to capture impact events in great detail from a variety of perspectives.

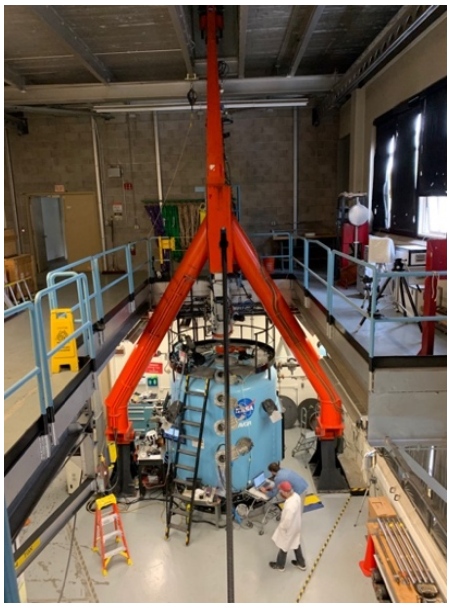

Fig. 6. Presents a photo of the AVGR facility, the blue structure is the vacuum chamber, the orange structure raises and lowers the gun. (Photo credit NRL/A. Nicholas).

The chamber has an internal diameter of 2.5 meters and is capable of reaching pressures as low as 0.5 torr at which all of our testing was performed. There is a large horizontal equipment platform that spans the inside of the chamber with a one-meter diameter well in its center. An impact target material is placed inside of the well to stop the projectile. The chamber has four viewing ports on the top of the chamber, four on the side of the chamber, and two large windows on the side of the chamber. These viewing ports can be configured with any of the facility's high speeds camera to observe the event.

The gun assembly can be configured as a single-stage powder gun or a two-stage light gas gun. The powder gun uses a gunpowder charge to launch the projectile at speeds up to 2.5 km/s. The first stage of the light gas gun uses a gunpowder charge to drive a piston which compresses pure hydrogen in the second stage. A burst disk is located at the end of the second stage to hold back the projectile until a high burst pressure is reached. The light gas gun can fire the projectiles of speeds up to 6.5 km/s. The gun assembly can be inclined in increments of 15° to launch projectiles at angles from 0° to 90°. A thin diaphragm can be placed at the end of the gun barrel to delay the hydrogen gas from entering the chamber while allowing the solid projectile to punch through.

The projectile materials used include spherical aluminum, alumina, borosilicate, quartz, and Pyrex among others. Single projectile diameters ranged from 1/16" to 1/4". The projectiles are set into a sabot with four fingers that grip the projectiles inside the gun's chamber. The sabot gives the projectile a uniform shape to maximize the speed and stability of the projectile. After the gun is fired, the projectile and sabot move through the gun's barrel while spinning

about the velocity axis. The spin causes the four fingers of the sabot to break apart and impact a cone shaped splitter which stops the sabot and allows only the projectile to continue through to the vacuum chamber.

### 4.2 Test Setup Geometry

The LARADO test setup frame was constructed from 80/20™ hardware and a 12" aluminum plate as the base. The setup includes: four cameras, two Ximeas and two Prophesees, and the laser sheet assembly. The cameras were positioned into two different views to simulate the expected viewing geometry on STPSat-7, a near parallel view and an isometric view as depicted in the chamber in Fig. 7. Ximea and Prophesee cameras were configured for each view. A 3-d model representation of the test setup is presented as Fig. 8, from top down the elements are the parallel Ximea camera, the collimator/diffusive optic, the parallel Prophesee camera, and the two isometric cameras (Ximea and Prophesee ganged in and out of page). Both parallel cameras were oriented approximately at a 10 degree towards the lasersheet. The isometric Ximea and Prophesee cameras were mounted on the same fixed and oriented 31.1 degrees up from horizontal. A photograph of the test setup is presented in Fig. 9.

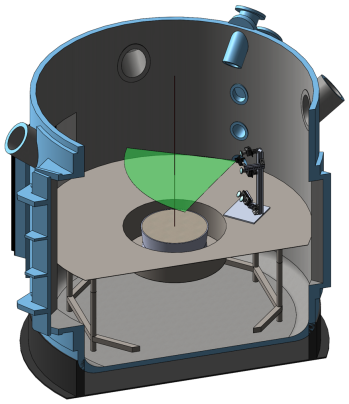

Fig. 7. A visual representation of the AVGR chamber.

The 30W nLight laser was mounted to a separate chiller plate that used a closed-circuit water loop to keep the laser from overheating. The water was circulated through the loop using a standard pond pump located just outside of the chamber. A custom feedthrough flange with two water tube feedthroughs was used to connect the pump to the chiller plate inside of the chamber. The laser's temperature was monitored during testing with the use of a thermocouple bonded to the base of the laser.

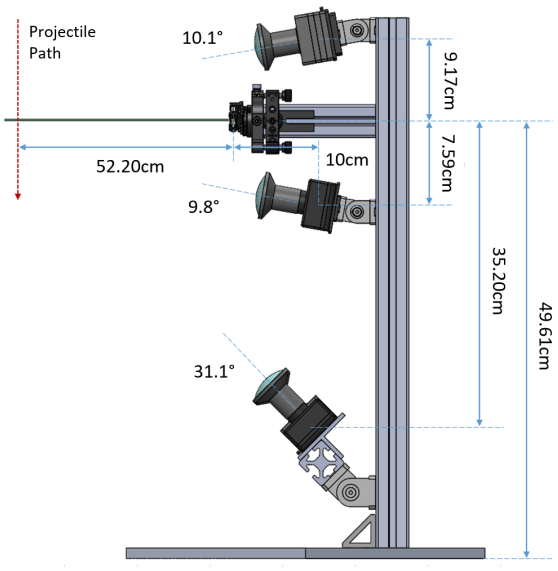


Fig. 8. Test geometry inside the AVGR chamber.

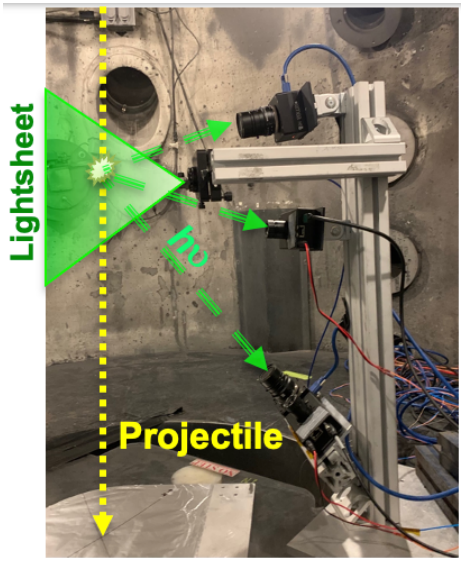


Fig. 9. The projection of the Ximea and Prophesee FOV onto the 45º wide lightsheet.

The focus and f/stop are manually adjusted to avoid saturation of the cameras at the laser intensity and frame rate employed. The intersection of the projected FOV with the lasersheet is shown in Fig. 10 for both the isometric Ximea and the isometric Prophesee cameras. The covered area is 1.901 $m^2$ and 1.386 $m^2$ respectively. The parallel cameras could observe the entire lasersheet.

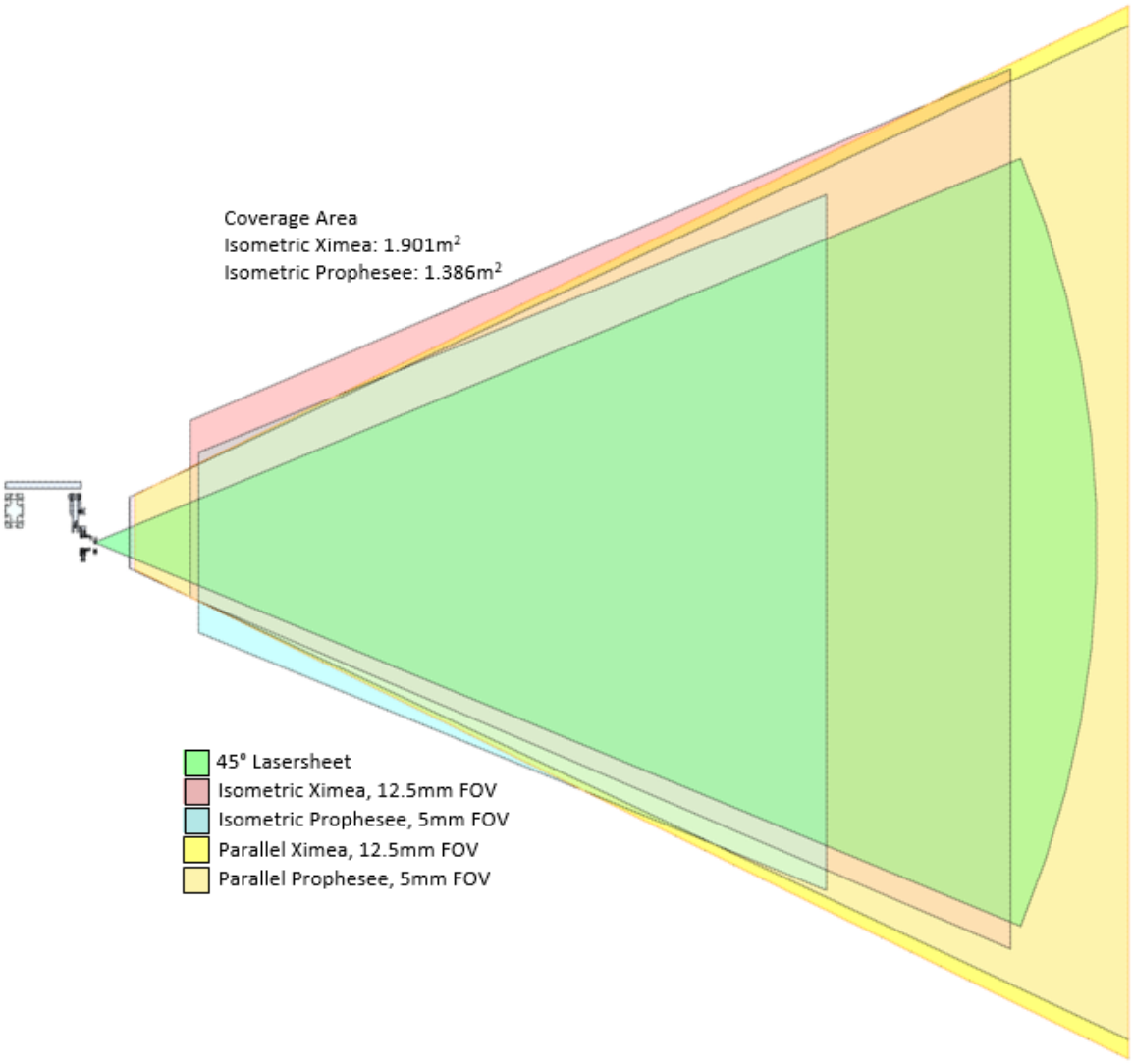


Fig. 10. The projection of the Ximea and Prophesee FOV onto the 45º wide lightsheet.

### 4.3 Laser

A survey of available laser and fiber optic combinations was made. Features sought were minimal size, weight, and power for future space flight opportunities. The laser must fit within the power, mass, and thermal budgets of a small spacecraft. In addition, spaceflight heritage was sought. Wavelengths compatible with COTS optics and sensors are also necessary. In the end, the nlight element™ E06 diode laser [7] operating at 793nm was chosen. This is a 30W CW laser that has spaceflight heritage from the ICESat-2 [8] and STPSat-5 HALO-net [9,10] missions. For the testing reported here the laser was operated at settings that produced 30W optical output.

### 4.4 The Lightsheet

The lasersheet assembly is composed of four components: an adjustable fiber collimator that collimates emitted laser light from a fiber optic cable, an adapter to mount the collimator, a diffusive optic that creates a fan-shaped sheet from the collimated laser light, and a 6-axis kinematic mount to position and orient components.

The laser light travels through a 105-micron multimode step index fiber to the focal point of a 11mm focal length collimating lens producing a collimated circular beam. The sheet generation method used a variation on a cylindrical

lens called a Powell lens. It is an improvement on a simple cylindrical lens and can be figured to produce uniform light sheets based on the laser beam diameter and intensity distribution [11,12,13]. Being made of glass, the lens is able to survive the 30W beam in vacuum without convective cooling. In addition to a rotary stage, it requires a lens holder and X and Y centering adjusters. The front face is manually adjusted to be normal to the collimated laser beam. Due to the early failure of the plastic engineered diffuser, the Powell lens system was used for all subsequent shots at AVGR in this test. The present Powell lens is 8.9 mm in diameter and is designed to produce a 45° fan beam (close to the expected 55° beam for STPSat-7, which was not yet determined at the time of the AVGR testing) for an input beam diameter of 4mm. Fig. 11 presents ray tracing results of the lightsheet generation system.

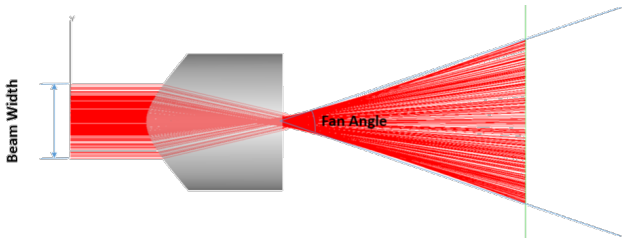


Fig. 11. Ray tracing of a collimated beam passing through a Powell lens.

A collimator lens of 11mm focal length collects the light from the NA ~0.15 output of the fiber optic and produces a collimated beam with diameter of 4mm and a divergence of 0.55°. The Powell lens spreads it to 45° in the horizontal dimension while leaving the vertical divergence at 0.55° from the collimator.

### 4.5 Ximea CCD Camera

One of the cameras chosen for the demonstration was a monochrome charge coupled device (CCD) progressive scanning camera manufactured by Ximea. The camera's model number is MD061MU-SY and is a part of Ximea's XiD family of USB3 cameras. The datasheet can be found online at: https://www.ximea.com/en/usb3-vision-camera/usb3-ccd-cameras-xid. The resolution of the camera is 2752 x 2202 pixels and can be cropped into a smaller region of interest (ROI) or pixel binned for faster readout speeds. It utilizes Sony's ICX814AL sensor chip which is 12.5mm by 10.0mm with each pixel within the sensor being 4.54µm. A photo of the camera is presented in Fig. 12. This camera uses C-mount lenses. The camera's dimensions are 60mm x 60mm x 37.2mm and has a mass of 320 grams without a lens attached. It has M4 mounting locations on the front, back, and bottom of the camera. The back of the camera can also couple to a heatsink to dissipate the camera's internal heat.

Fig. 12. The Ximea XiD CCD camera model MD061MU-SY.

The camera output is capable of resolutions of 8, 10, 12, or 14 bits per pixel. The sensor can be split into 1, 2 or 4 sensor regions (TAPs) to increase the readout speed. Each TAP utilizes its own analog to digital convertor. Setting a region of interest (ROI) also can speed up the readout. A subset of the camera's pixels can be selected for readout by providing a width, height, x offset, and y offset of the desired region. When decreasing the number of horizontal rows being read out, the CCD can quickly skip over unwanted rows. Vertical ROI adjustments are completed on the software side and do not provide increased readout speed. Individual pixels can also be combined into super pixels using the binning process. Square pixel groups of up to 5x5 can be created with the individual pixels values in each group being summed or averaged.

### 4.6 Prophesee Neuromorphic Camera

An event-based, or neuromorphic, camera [14] is based on a sensor that only records changes in brightness of the observed scene. Unlike conventional frame-based cameras, a neuromorphic camera does not capture image frames using a shutter, rather each pixel operates independently only reporting changes in brightness for that pixel as they occur. The camera's output, for each individual pixel, a 1 for an increase in brightness above a set threshold, a 0 for a decrease in brightness below an independently set threshold, or no output if the brightness remains unchanged. Each pixel responds asynchronously to changes in brightness as they occur [15]. A comparison between a reference brightness for each pixel from the last event and the current brightness is used to determine if an event occurred. If that brightness increased (or decreased) above (or below) a set threshold, an event is generated with a timestamp, pixel location, and polarity (increase or decrease, 1 or 0) [16]. The reference value for that pixel is then reset to the last

observed brightness and the comparisons continue. Each pixel is capable of measuring illumination changes in a scene at high speeds (μs).

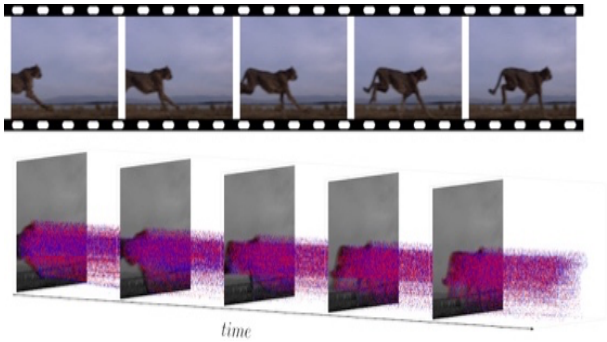


Fig. 13. How a neuromorphic camera works compared to a traditional frame camera.

The use of a neuromorphic camera the orbital debris application has several advantages including high speed output, large dynamic range, and reduced data bandwidth. This technology is well-suited for fast impulsive event detection above a background scene as is expected with small orbital debris passing through the LARADO lightsheet at 8 to 15 km/s. In a traditional frame-based camera, such as the Ximea, a frame is collected over a set exposure period. For the AVGR testing the Ximea exposures were set to 40 ms. The debris spends about 1 ms in the lightsheet. This means that in the traditional frame camera, the signal of from the debris is exposed for a <1ms while the background of the scene is exposed 40 times longer.

The observations of a neuromorphic camera are depicted in Fig. 13 where the pink (increases in brightness) and blue (decreases) dots represent the continuous motion of a cheetah super imposed between frames from a traditional camera. The high-speed nature of a neuromorphic camera provides a tremendous advantage

over the traditional frame-based cameras. However, due to the fact that the neuromorphic camera does not report the actual brightness it is limited in the amount of characterization of the debris (was it bright or dim?) it can measure. For our laboratory work the Prophesee 4.1 HD camera, based on the Sony MX636 1/2.5-type chip, was selected. This camera, shown in Fig. 14 has 1280 x 720, 4.86-micron pixel resolution and uses a USB 3 interface.

Fig. 14. The Prophesee 4.1 HD neuromorphic camera.

### 4.7 AVGR Data

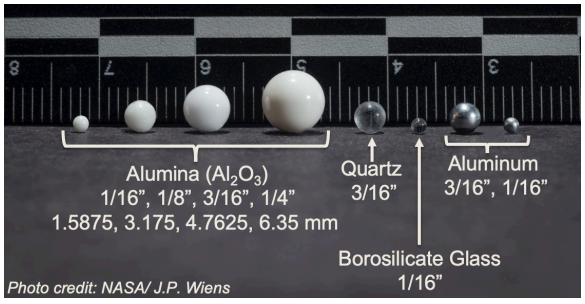


Figure 15. Photo of projectiles used during this testing at AMES. Photo credit NASA /JP Wiens.

In total, twenty shots were taken over a test period of five days at the AVGR facility. Six shots were taken with the powder gun (PG), twelve shots were taken with the light gas gun (LGG), and additional two LGG shots were taken in an alternate configuration for an application on the surface of the moon. Table 3 provides the shot matrix providing gun information, particle size (diameter in both inches and mm), speed and material. A photo of the actual projectile types and sizes is presented in Fig. 15, from left to right the first four are alumina, the next two are quartz and borosilicate glass, and the final two are aluminum. Our first round of testing at AVGR used all of these projectiles [17], the second week of testing at AVGR focused on 1/8" and 1/16" alumina and aluminum projectiles as well as two shots with sand and 0.5mm diameter polyethylene spheres.

**Table 3. AVGR Trip 2 Shot Test Matrix**

| Shot # | Gun | Projectile Diameter | Velocity (km/s) | Material |
|---|---|---|---|---|
| 1 | PG | 1/8" (3.175 mm) | 2.33 | Alumina |
| 2 | PG | 1/8" (3.175 mm) | 2.37 | Alumina |
| 3 | PG | 1/8" (3.175 mm) | 2.3 | Alumina |
| 4 | PG | 1/8" (3.175 mm) | 2.31 | Alumina |
| 5 | PG | 1/8" (3.175 mm) | 2.31 | Alumina |
| 6 | PG | 1/8" (3.175 mm) | 2.37 | Alumina |
| 7 | PG | 1/8" (3.175 mm) | 2.31 | Alumina |
| 8 | PG | 1/8" (3.175 mm) | 2.32 | Alumina |
| 9 | PG | 1/8" (3.175 mm) | 2.32 | Alumina |
| 10 | PG | 1/8" (3.175 mm) | 2.27 | Alumina |
| 11 | PG | 1/8" (3.175 mm) | 2.33 | Alumina |
| 12 | PG | 1/8" (3.175 mm) | 2.3 | Alumina |
| 13 | PG | 1/8" (3.175 mm) | 2.3 | Alumina |
| 14 | PG | 1/8" (3.175 mm) | 6.27 | Alumina |
| 15 | LGG | 1/8" (3.175 mm) | 6.27 | Alumina |
| 16 | LGG | 1/8" (3.175 mm) | 6.3 | Aluminum |
| 17 | LGG | 1/8" (3.175 mm) | 4.64 | Aluminum |
| 18 | LGG | 1/16" (1.5875 mm) | 6.58 | Alumina |
| 19 | LGG | 1/16" (1.5875 mm) | 6.42 | Aluminum |
| 20 | LGG | 1/16" (1.5875 mm) | 6.49 | Aluminum |
| 21 | LGG | 1/16" (1.5875 mm) | 6.41 | Aluminum |
| 22* | LGG | various | 4.76 | Sand |
| 23* | LGG | 0.5 mm | 4.72 | Polyethylene |

***Shots 22 & 23 were cup carriers with multiple objects**

### 4.7.1 Ximea Data Analysis

The Ximea CCD camera images are processed to determine the frame in which the simulated debris crossing event occurs. Once that frame is identified an image difference between the event frame and the previous frame is calculated. This technique helps to reduce the background for the rest of the scene and make the impulsive debris event stand out. This process is presented in Fig. 16 for a shot from the first week of AVGR testing. The upper left image is a cropped (800 x 800) image of the event frame centered on the expected projectile crossing location in the bottom half of the image, chamber structure is clearly visible. The ¼" projectile is clearly seen at the center of this image. The image on the upper right is the last image acquired prior to the debris event. An image difference was calculated, Event Frame minus Previous Frame, and is presented in the lower left panel. The difference image isolates the signal from the debris event. The lower right panel contains a zoomed (100 x 100) differenced image centered on the projectile. This method was applied to each of the shots from the second week of AVGR testing, zoomed (100 x 100) differenced images are presented in Fig. 17 for the parallel view and Fig. 18 for the isometric view for each of the 23 shots taken during the second week of testing at AVGR.

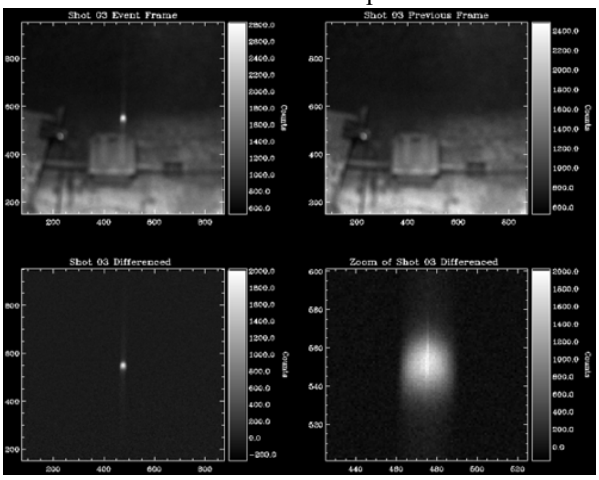


Figure 16. Image differencing process.

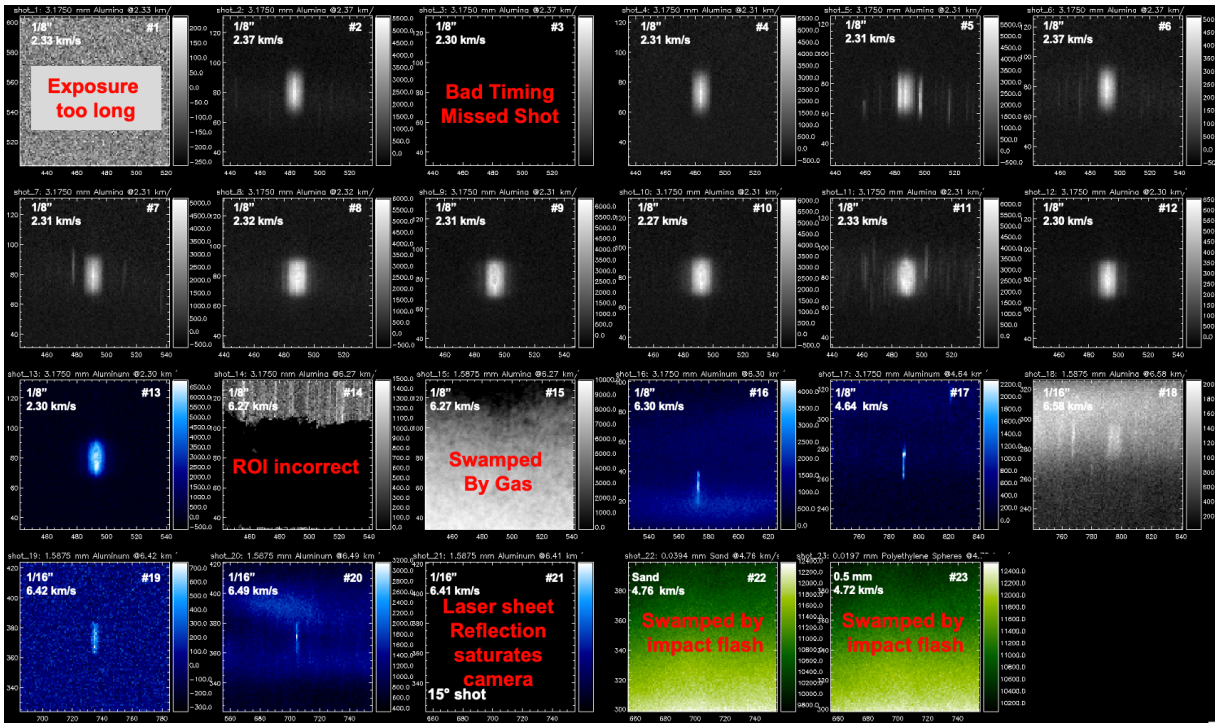


Fig. 17. Cropped (100 x 100) differenced images (event frame minus previous frame) from the Ximea parallel camera for shots 1 through 23. Greyscale images are alumina, blue are aluminum and green are sand or poly.

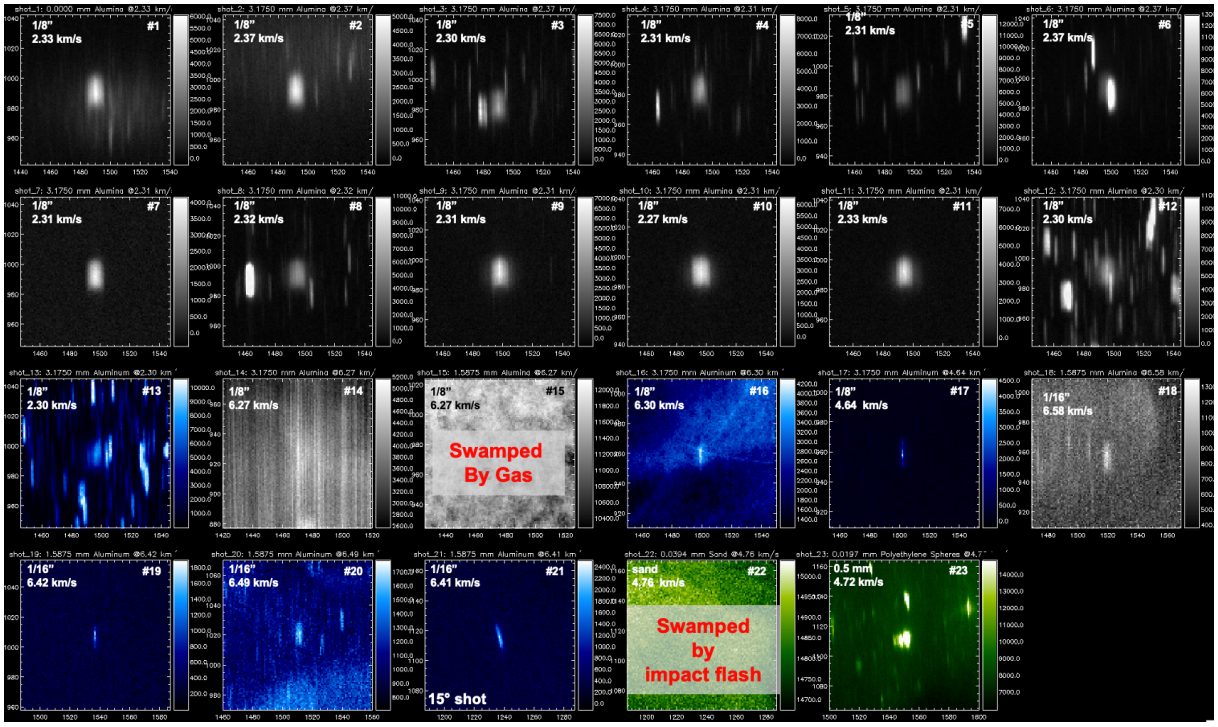


Fig. 18. Cropped (100 x 100) differenced images (event frame minus previous frame) from the Ximea isometric camera for shots 1 through 23. Same color scheme as Fig. 17.

The first twelve shots were 1/8" alumina from the powder gun, all with a very strong signatures in both the isometric and parallel views. The parallel Ximea was overexposed, 40 ms instead of 14 ms, on the first shot and the timing was off on the third shot. The isometric Ximea was set to 40 ms for all shots. The region of interest was incorrectly set on the parallel Ximea for shot 14 and the projectile lightsheet crossing point was not in view. In the Ximea differenced images the projectiles are visible as are other particles consisting gunpowder from the shots and upward moving debris ejected from the impact of the projectile with the polyethylene backstop. A cross-section of a polyethylene cylinder after several impacts is shown in Fig. 19. The ejecta moving upward and outward from the polyethylene cylinder is slower and thus they often provide more signal that the actual projectile because they spend more time in the lightsheet. Signal levels expectedly decrease with increasing object speed and increase with increasing albedo; however, the different projectiles provide a variety of surfaces such that the observed signal of the projectile in the sheet can appear Lambertian, specular or a mix of the two. The alumina projectiles display a specular (especially evident under 3 km/s) and Lambertian response while the aluminum are mostly specular in response. As in the previous testing [17], analysis of the pixel width of the observed responses confirm that computed spatial information is consistent with particle size for projectiles with Lambertian responses. The widths of the observed signal in shots 11 and 18 are 10 and 5 pixels respectively, a 2:1 ratio to the actual projectile diameters of 1/8" and 1/16". These relative spatial sizes indicate that the observations are capturing the full width of the projectile. The measured plate scale for this setup is 0.16mm/pixel at the projectile's crossing point with the lightsheet.

Figure 19. A cross-section of one of the polyethylene backstops taken after multiple shots. Photo credit NASA /JP Wiens.

An analysis from each event was performed to determine the background subtracted total signal in each event. This was accomplished by calculating a nearby average background level for each pixel, summing the counts from the projectile response and subtracting off the product of the average background times the # of pixels in the observed projectile event.

### 4.7.2 Modelling

To better predict what the LARADO instrument will see on orbit, a performance model was created that simulates both on-orbit and laboratory images captured with the Ximea camera. The model includes many tunable parameters, such as particle velocity, size, and albedo as well as laser power. The model produces expected images for both parallel and isomorphic views of the laser sheet.

The model begins by assuming a spherical pellet Lambertian reflectance completely penetrating an infinitely thin laser sheet in one image collection time. This is a reasonable assumption as for STPSat-7 the laser sheet will be perpendicular to the ram direction and most particles that penetrate the sheet will be moving quite rapidly with respect to the satellite. Using these assumptions, we can determine the total photons reflected back to a camera for every point in the laser sheet, as seen in Figure 20. This model run is for the STPSat-7 geometry with a 55 deg lightsheet emitting 30W of laser power at 793 nm. The debris modeled is a 1/16" diameter alumina pellet moving at 10 km/s.

$$S_C(R, r_P, D_R, v_p, \eta_P) = C_0\, P_0\, \frac{360^\circ}{\theta_{PL}}\, \varepsilon_L\, r_P^2\, \eta_P\, A_{eff}\, \varepsilon_C\, \frac{1+\frac{R^2+D_R^2-P^2}{2\,R\,D_R}}{2\,R\,v_p\,D_R^2}$$

The signal ($S_C$) from the debris passing through the lightsheet is a function of penetration distance along lightsheet ($R$), particle (debris) radius ($r_p$), distance from camera to intersection point ($D_R$), the relative velocity of the particle with respect to the lightsheet ($v_p$), albedo ($\eta_P$). The other terms are constant for a fixed wavelength laser and camera efficiencies where $C_0$ is a constant term that incorporates the laser wavelength, laser power ($P_0$), Powell lens angular extent ($\theta_{PL}$) and efficiency ($\varepsilon_L$), and camera effective aperture ($A_{eff}$) and efficiency ($\varepsilon_C$). The observed illumination phase term is the numerator or the final term.

These total signal values from the Ximea shots are listed in Table 4 along with the modeled response for each event based on the projectile size, velocity, geometry, lasersheet output and an albedo of 1 (we are still working on lab measurements of projectile samples).

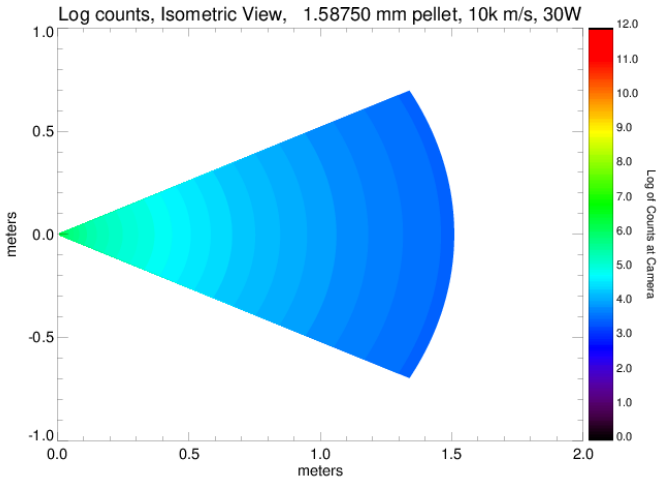


Fig. 20. Modeled isometric camera response for STPSat-7 configuration.

**Model Results AVGR2**

| Shot # | Size (mm) | Velocity (km/s) | Total Counts Observed Isometric | Modeled Signal (Total Counts) Isometric | Total Counts Observed Parallel | Modeled Signal (Total Counts) Parallel | Material |
|---|---|---|---|---|---|---|---|
| 1 | 3.175 | 2.33 | 985934 | 1128000 | N/A | 1770000 | Alumina |
| 2 | 3.175 | 2.37 | 726345 | 1110000 | 982207 | 1688000 | Alumina |
| 3 | 3.175 | 2.3 | 455712 | 1144000 | N/A | 1738000 | Alumina |
| 4 | 3.175 | 2.31 | 657231 | 1138000 | 914089 | 1732000 | Alumina |
| 5 | 3.175 | 2.31 | 693268 | 1138000 | 1101090 | 1732000 | Alumina |
| 6 | 3.175 | 2.37 | 1873720 | 1110000 | 957225 | 1688000 | Alumina |
| 7 | 3.175 | 2.31 | 558515 | 1138000 | 827091 | 1732000 | Alumina |
| 8 | 3.175 | 2.32 | 873320 | 1134000 | 1590270 | 1724000 | Alumina |
| 9 | 3.175 | 2.32 | 1336580 | 1134000 | 1636280 | 1724000 | Alumina |
| 10 | 3.175 | 2.27 | 1310370 | 1158000 | 1656180 | 1762000 | Alumina |
| 11 | 3.175 | 2.33 | 1328600 | 1128000 | 1715730 | 1770000 | Alumina |
| 12 | 3.175 | 2.3 | 866629 | 1144000 | 1586250 | 1738000 | Alumina |
| 13 | 3.175 | 2.3 | 609420 | 1144000 | 1646420 | 1738000 | Aluminum |
| 14 | 3.175 | 6.27 | N/A | 420000 | N/A | 624000 | Alumina |
| 15 | 3.175 | 6.27 | N/A | 420000 | N/A | 624000 | Alumina |
| 16 | 3.175 | 6.3 | 66739 | 418000 | 152549 | 634000 | Aluminum |
| 17 | 3.175 | 4.64 | 117409 | 566000 | 50364 | 862000 | Aluminum |
| 18 | 1.5875 | 6.58 | 36023 | 100000 | 150599 | 152000 | Alumina |
| 19 | 1.5875 | 6.42 | 39484 | 102400 | 34639 | 155800 | Aluminum |
| 20 | 1.5875 | 6.49 | 33569 | 101200 | 76318 | 154000 | Aluminum |
| 21 | 1.5875 | 6.41 | 94513 | 102600 | N/A | 156000 | Aluminum |
| 22* | various | 4.76 | NA | N/A | N/A | N/A | Sand |
| 23* | 0.5 | 4.72 | NA | 13800 | N/A | 21000 | Polyethylene |

***Shots 22 & 23 were cup carriers with multiple objects**

There were three consecutive shots where the images were very clean, minimal gunpowder and/or gas in the event frame (as we expect for our on-orbit data), and low backgrounds; these where Ximea isometric views from shots 9, 10, and 11. The background subtracted total count analysis of these frames is shown in Fig. 21. These compare well with the modeled count rates with ratios of observed to modelled values of 1.18, 1.13, and 1.18 respectively.

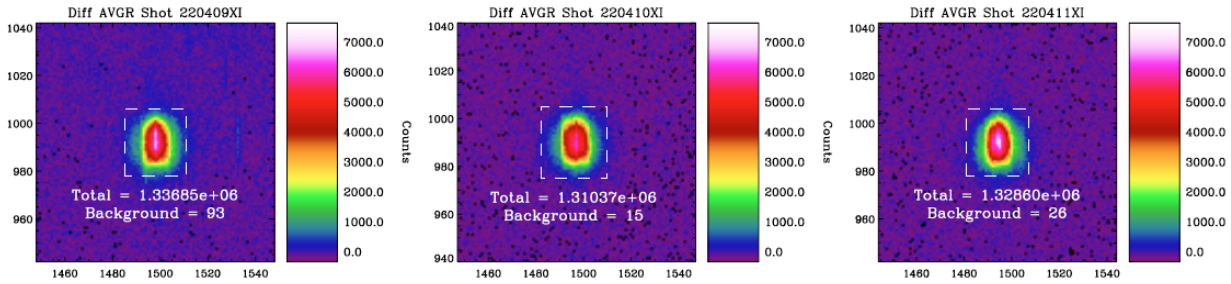


Fig. 20. Background (counts/pixel outside the dashed box) subtracted total event (inside the dashed box) analysis for Ximea Isometric view shots 9, 10, and 11. Future work on the model will be an upgrade to model the thickness of the lasersheet.

### 4.7.3 Ximea Event Detection

NRL is working on several image processing techniques to auto-detect events in LARADO data, including difference thresholding and other traditional image processing techniques. On STPSat-7, the parallel camera on-board event detection algorithms will trigger the download of both the parallel and isometric views. Development of these algorithms has begun. The initial philosophy is to auto-detect a frame with a debris event with minimal processing so that the algorithm can run in real-time. The differenced images are computed and then the mean value of the differenced images is calculated. These mean values for each frame are then compared to a threshold value, which can be determined by analyzing baseline data (from the laboratory or during early orbit testing for STPSat-7).

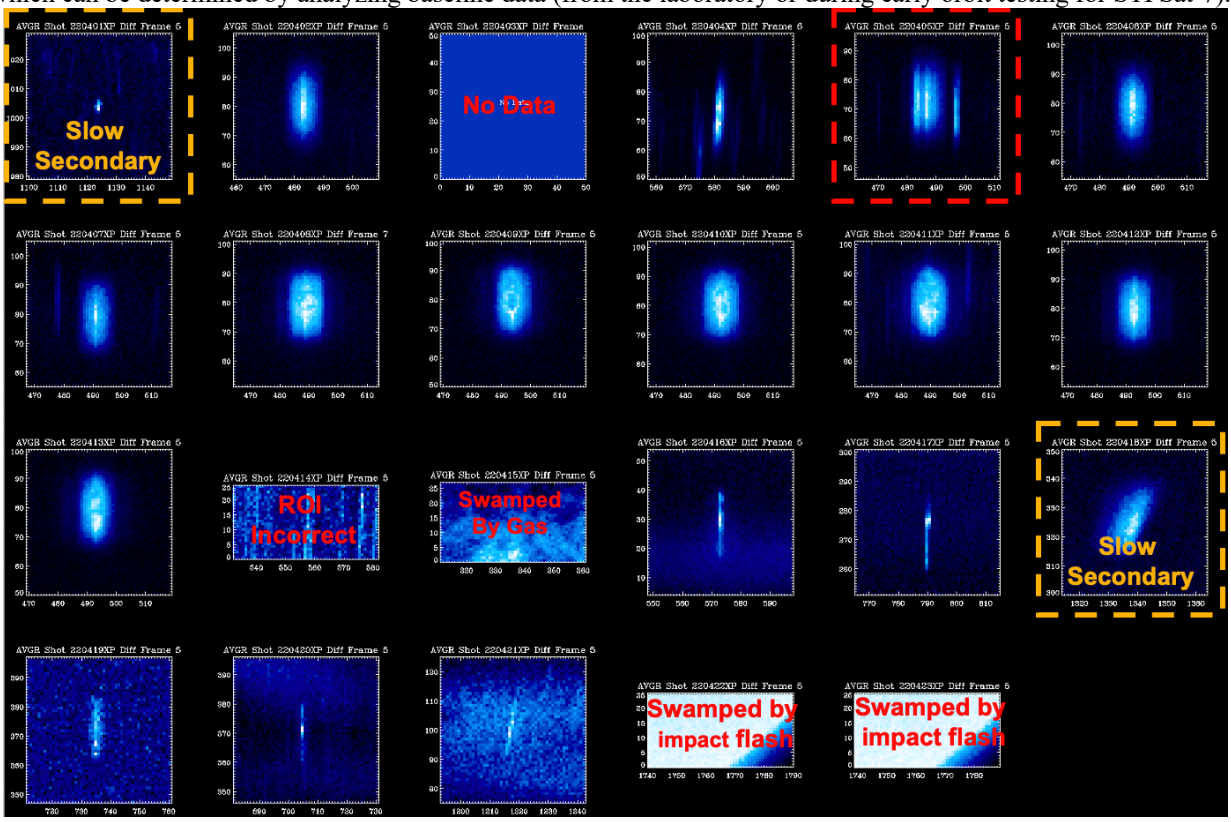


Fig. 22. Autodetection results for Ximea Parallel data. Event frame successfully identified in 21 of 22 events (red highlighted frame (#5) was incorrectly identified as event frame). Successfully identified 16 of 19 single projectile events. Yellow highlighted frames (#1 & #18) incorrectly identify slow secondary ejecta and frame #15 was swamped by gas.

Differenced frames with mean count rates above the threshold is used to identify the time of the event and several frames (±3 to ±7) around the event time are then flagged for download along with their isometric view counterparts. The technique was applied to the AVGR Ximea data, in which 21 of 22 event frames were properly identified in the data set. Shot sequence four incorrectly identified the event frame (it was one frame too late). Once the event frame is identified the event location is determined by finding the peak pixel of the differenced image. This technique was successful on 16 of 19 event frames from single projectile images in shots 1, 2, 3-12, 15-21. The sequence from Shot 3 had a timing offset such that the event frame was not recorded and during shot 14 the region of interest was incorrectly set. Fig. 22 presents the auto-detected events using the two-step threshold-peak process. The two events that were mis-identified, shots 1 & 18 were both cases where slow moving ejecta from the impact were observed moving through the lightsheet. This is not expected on orbit, as we expect single debris events during the 13-ms exposure. The algorithm needs to be tested for scenes with stars, the moon and planets. We are currently testing algorithms in python on evaluation boards similar to the flight processors.

### 4.7.4 Neuromorphic Data Analysis

Due to the continuous streaming nature of the neuromorphic data as described in a previous section, it is necessary to visualize data such that it may be physically interpreted. This is accomplished through integration time intervals where all occurring events are viewed together as a "composite frame" with an associated "frame rate" much like that of a traditional CCD with an exposure duration and conventional frame rate. In order to maximize probability and clarity of detection, these parameters are taken at the Prophesee MetaVision™ processing software limits of 100 µs integration frames reported at 10,000 FPS (1/100 µs).

Fig. 23 displays a collage of all shots from the field of view of the parallel neuromorphic camera. Data is shown for all initial responses to the shots including both positive detection cases and other camera reactions with labels for shot conditions including material, size and velocity. Cases listed as "Camera Connection Failure" represent shots where the camera was not able to report data and are unrelated to the shot test conditions.

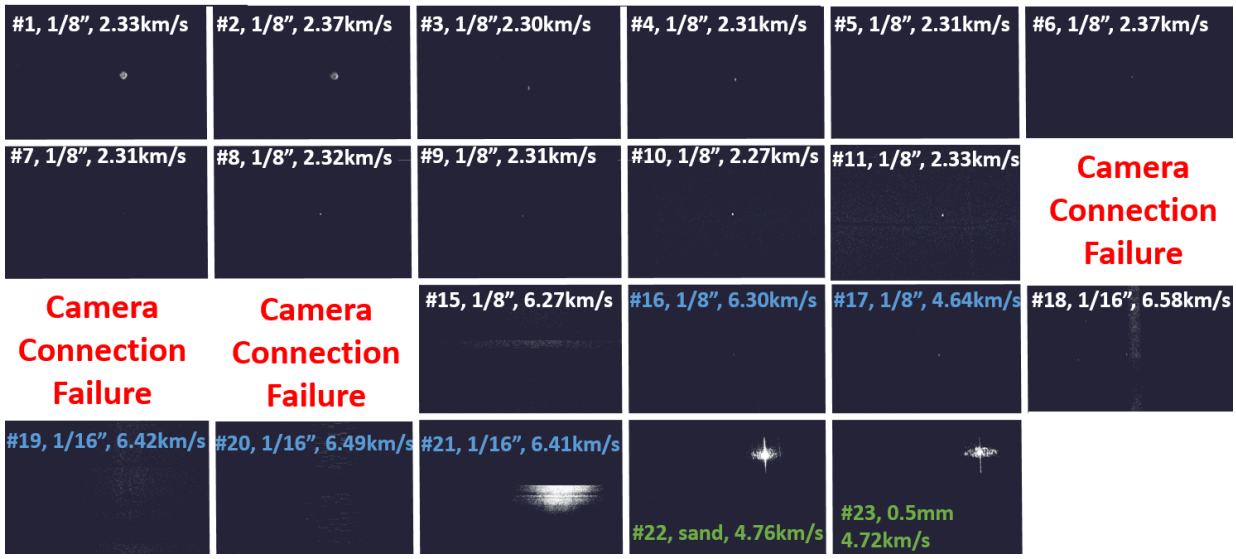


Fig. 23. Presentation of neuromorphic data from the parallel camera view.

Positive detections are more easily seen in shots 1-4, 6, 8, 10, 11, 16, 17 with more faint detections on shots 5, 7, 19 that are shown in an enhanced view in Fig. 24 As a validation, Fig. 25 displays a detection comparison between the neuromorphic view and NASAs Phantom high-speed camera taken from a similar view angle. Shots 1 and 2 of Fig. 23 show non-physically large, near perfect circle detections. This has been determined to be an optical result of attempting to use a narrow band filter within the optical channel of the camera. Our primary hypothesis for this type of image is that due to multiple reflections within the lens/filter assembly, the result of which is an image of the lens iris on the detector with constant size. These filters were removed from both neuromorphic cameras for all subsequent shots in an effort to produce the most well-defined projectile images as possible.

It is interesting to note the unusual camera behavior seen in shots 15, 20 and 21 of Fig. 23. Large batches of horizontal pixel groups are illuminated with sharp vertical cutoffs. We believe this behavior, though intermittent, is due to the high energy shock of the projectile impact flash with the target and is never observed during lower velocity (< 6km/s) cases. Though these conditions will not be encountered on orbit, we are pursuing mitigation techniques to enhance our ground-based testing and development that will be discussed in a following section.

The sand/polymer cluster shots 22 and 23 show a remarkable and similar spinning top shape appearance. The widened cloud of the smaller particulates appear narrow vertically in signature as they pass through the thin laser sheet. Centered in the cloud is a large bright detection corresponding to the "cup" that carried the debris along with it.

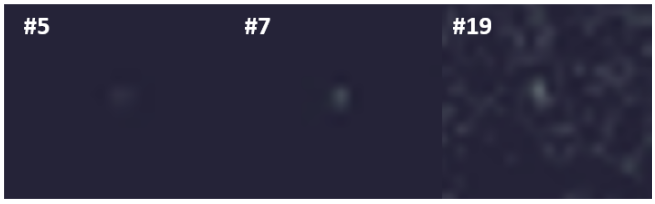


Fig. 24. Enhanced views of weak projectile detections from the neuromorphic parallel view.

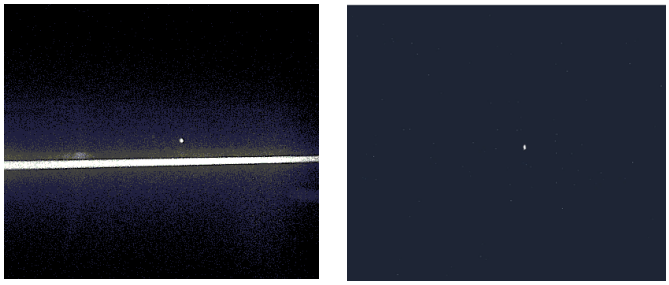

Fig. 25. Example comparison of NASAs Phantom high-speed camera (Left) with the parallel neuromorphic view (Right).

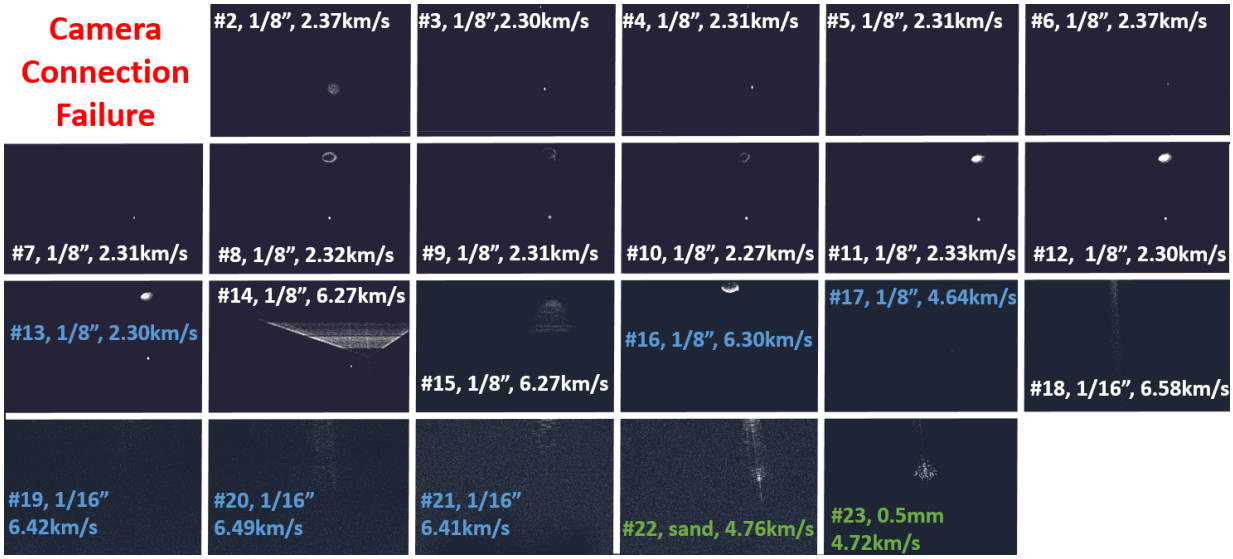


Fig. 26. Presentation of neuromorphic data from the isometric camera view.

Fig. 26 shows the corresponding collage of shot data for the isometric neuromorphic camera view. Here we see a disc like feature in shots 8-13 and 16 not observed previously by the parallel camera view. This disc is aperture of the gas delay box system which is otherwise out of view from the parallel camera. Though this delay structure was present for the preceding shots 1-7, the signature of the aperture cut appears in cases that it has been first sealed with tape in an effort to further limit the effective aperture when the projectile passes through and limit gas flux seen by the cameras. The entire aperture appears illuminated as the tape is shocked much like a drumhead due to the penetration of the projectile. Further appearance of the gas delay system can be seen in shot 14 where the top panel (camera is looking slightly upwards) has in view an illumination of the top corner of the confined system. The gas delay box was removed from the test configuration after shot 16.

The environmentally driven quality of observations made by the isometric view closely resemble those from the parallel view as expected. Examples include: the filter induced blooming in shot 2, the faint but measurable detection in shot 5, system shock in shots 15, 20, and 21, and even the collimated gas stream seen in shot 18.

It can be seen from Fig. 26 that the isometric view is successful in making clear detections of individual projectiles for all lower velocity cases (<6 km/s) though appears to have difficulty with the higher energy cases (with the exception of shot 14). This may be due to the camera position relative to the impact target. As shown in the geometry of Fig. 8 this camera is located much closer to the impact and is more likely to suffer the effects of system shock as opposed to the more separated parallel camera.

In an effort to increase detectability, a variety of camera tuning parameters were explored. These parameters include threshold values for pixel reporting, frequency filters and pixel refresh rate. They are tunable to allow the end user to tailor performance for specific application. To examine this, shot conditions were kept relatively constant for shots 1-12. Fig. 27 displays the settings used for each shot along with the bias parameter definition. Note that the bias values have no well-defined units. For that reason, parameters in general were taken to minimum/maximum allowable values to observe any potential effect.

Inspection of the constant shots 3-12 (note: all include the gas delay system) in Fig. 26 show slight variations performance though no immediately apparent "favorite" condition. Perhaps the most significant effect is seen in enhanced views of the parallel camera shots 7, 9 and 10 from Fig. 23. Shots 7 and 9 share identical bias conditions and are consistent with each other in faint detections. Whereas the independent variation of our high pass filter condition in shot 10 shows a more pronounced image. The result of this varying condition can be seen in Fig. 28.

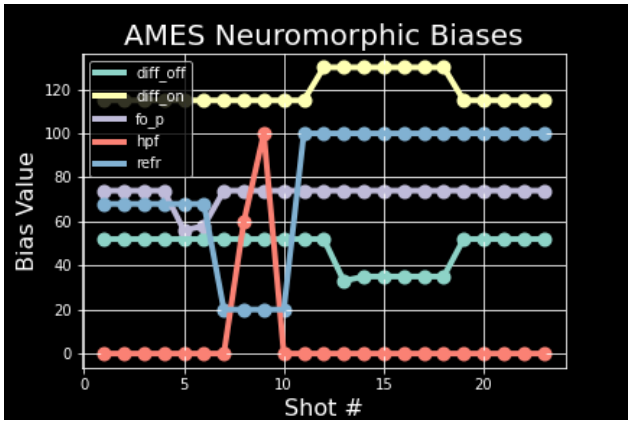


| Bias Name | Meaning |
|---|---|
| Diff_off | Threshold for off pixel reporting |
| Diff_on | Threshold for on pixel reporting |
| Fo_p | Low–pass cut-off frequency |
| Hpf | Hi-pass filter |
| Refr | Pixel refresh rate |

Fig. 27. Setting values of bias parameters of the neuromorphic cameras for each shot. Bias value names and definitions are shown in the legend on the right.

Overall, it was found that variations from default settings tended to result in diminished performance and with time and resource limitations a more thorough investigation could not be completed. Additional camera settings including event rate control (a throttling of the camera throughput) and inclusion of a region of interest were investigated to assist potentially mitigating camera saturation due to the high energy system shocks. These parameters too had no discernable effect here though we have observed they are useful in other noisy background environments to limit camera saturation limits and resulting camera crashes.

Due to the data downlink bandwidth limitations associated with space flight operations, it is necessary to limit data collection to only that which is of interest. Based on previous analysis [5] for the orbit selected on STP-Sat7 we only expect on the order of a single debris conjunction per day. In order to limit the science data saved for downlink whilst continuing to look for conjunctions we seek to implement an autodetection scheme to report positive events.

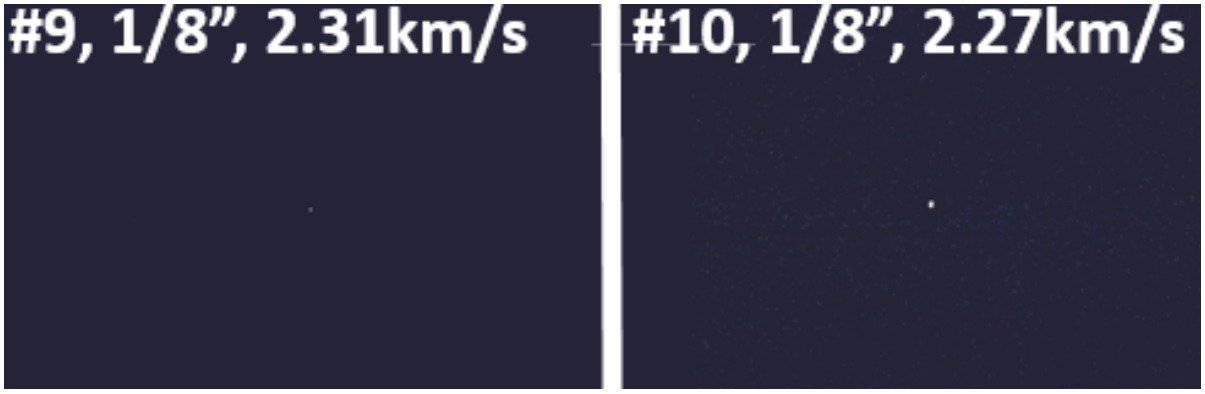


Fig. 28. A comparison of the parallel neuromorphic images with variations of the high pass filter parameter.

We implement this functionality using modules from the commercially available Prophesee Metavision™ software suite, from the same manufacturer as the Prophesee neuromorphic cameras. Clusters of pixel reporting events are intelligently identified as objects for which an identification number, time, size and position in the field of view are cataloged. Though due to the speed through the spatially thin laser sheet is too high to register a debris object in multiple “equivalent frames”, the software package does have the capability to continuously track objects whilst retaining their unique identifiers. This may prove useful in the tracking and following rejection of slow-moving background objects such as stars. Fig. 29 shows an example autodetected shot with conditions of a 1/16” alumina sphere traveling at 6.38 km/s. The software algorithm has positively identified the object, surrounded it in a rectangular pixel space, and given it the expected first identifier as object 0 meaning there were no false positive detections prior.

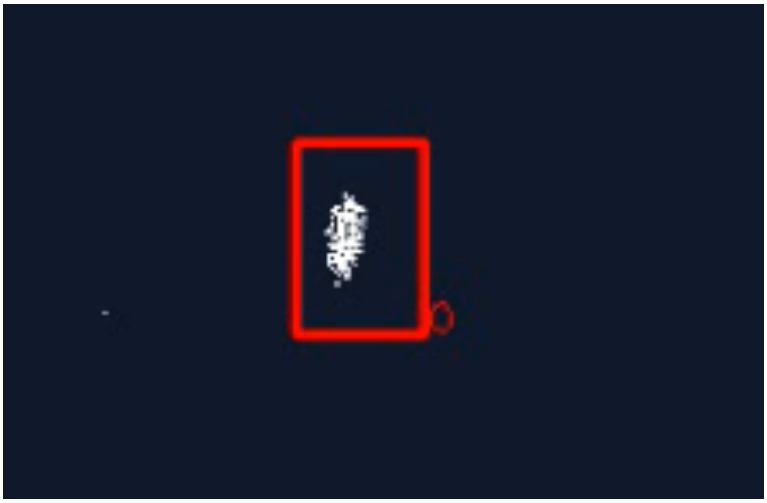

Fig. 29. Example of a software autodetected 1/16” alumina sphere traveling at 6.38 km/s correctly identified and sized with no prior false positives from the background environment.

## 5. CONCLUSIONS

The lasersheet technique has been verified using small projectiles at near orbital velocities. Detections were made of projectiles ranging from 1/8” to 1/16” (3.175 mm to 1.59 mm diameter) moving at speeds of 2.30 kms to 6.58 km/s. The fastest observation was a 1/16” (1.59 mm) alumina projectile moving at 6.58 km/s (shot 18). The smallest object detected was a 0.5 mm polyethylene sphere moving at 4.72 km/s (shot 23). This work has significantly increased the technological readiness level (TRL) of the sensing technique to TRL 6 on the NASA scale. Future plans include frame-by-frame analysis of the AVGR witness camera images, continued modelling of the events, optimization of the observational setup (goal of reducing the background gas in the event scene) and work on detection algorithms. The neuromorphic cameras seem well-suited for debris detection, however, even though current timelines restrict use on STPSat-7 potential use in future instruments exists and testing will continue. The LARADO instrument team is working towards the sensor Critical Design Review (CDR) in the fall of 2022 for the instrument on the STPSat-7 spacecraft, an ESPA class vehicle that will have a 500 km circular orbit at an inclination of 60 degrees. Launch of STPSat-7 is slated for early-mid 2024.

## 6. ACKNOWLEDGEMENTS

The authors would like to acknowledge NASA's Heliophysics Division's nascent Orbital Debris and Space Situational Awareness activity within NASA's Science Mission Directorate for the funding the LARADO program. The authors would also like to acknowledge the DoD Space Test Program for developing the STPSat-7 mission, including spacecraft development and integration, launch and one year of on-orbit operations. The authors would like to thank the crew at the NASA AVGR facility for their help and insight in the use of that facility.

## 7. REFERENCES

[1] NASA, Monthly number of objects in Earth orbit by type, Orbital Debris Quarterly News, Vol. 26 Iss. 1, March 2022.

[2] R. Crowther, Space junk-protecting space for future generations, Science 296 (5571) (2002) 1241-1242.

[3] National Aeronautics and Space Administration. "Process for Limiting Orbital Debris," NASA-STD-8719.14A (with Change 1), approved 2011-12-08.

[4] C. Englert, et al., Optical Orbital Debris Spotter, Acta Astronautica, 104 (2014), 99-105.

[5] A. Nicholas, C. Englert, C. Brown, T. Finne, K. Marr, C. Binz, L. Healy and S. Kindl. "Lightsheet Sensor for the Detection of Orbital Debris." International Conference on Orbital Debris, 6036, (2019).

[6] J. Karcz , D. Bowling, C. Cornelison, A. Parrish, A. Perez, G. Raiche, and J.P. Wiens, "The AMES Vertical Gun Range", 47th Lunar and Planetary Science Conference, 2599, (2016).

[7] nLight element e06 data sheet, https://www.nlight.net/semiconductor-lasers-products/element-e06-fiber-coupled-diode-laser-scph6

[8] N. Sawruk, et. al., "Space certification and qualification programs for laser diode modules on the NASA ICESat-2 Mission," Proc. SPIE 8872, Lidar Remote Sensing for Environmental Monitoring XIV, 887204 (17 September 2013); doi: 10.1117/12.2026253.

[9] D. Wayne, D. Obukhov, K. Brook, and M. Lovern, "A Large Aperture Modulated Retroreflector (MRR) for CubeSat Optical Communication," AIAA/USU Conference on Small Satellites," Logan, Utah (2014).

[10] D. Wayne, D. Obukhov, A. Phipps, M. Tran, K. Brook, and M. Lovern, "Design and Testing of a CubeSat-Sizes Retroreflector Payload," AIAA/USU Conference on Small Satellites, SSC15-P-40 Logan, Utah (2015).

[11] Laserline Optics Canada, Inc. https://www.laserlineoptics.com/store/product/powell-lens/ https://www.laserlineoptics.com/powell_primer.html https://www.laserlineoptics.com/powell_primer.html

[12] I. Powell, "Design of a laser beam line expander," APPLIED OPTICS, 26 3705 (1987).

[13] A. Bewsher, I. Powell, and W. Boland, "Design of single-element laser-beam shape projectors," Appl. Opt. 35, 1654-1658 (1996).

[14] H. Li; H. Liu; X. Ji; G. Li; L. Shi, (2017). "CIFAR10-DVS: An Event-Stream Dataset for Object Classification". Frontiers in Neuroscience. 11: 309. doi:10.3389/fnins.2017.00309. ISSN 1662-453X. PMC 5447775. PMID 28611582.

[15] P. Lichtsteiner; C. Posch; T. Delbruck, (February 2008). "A 128×128 120 dB 15μs Latency Asynchronous Temporal Contrast Vision Sensor" (PDF). IEEE Journal of Solid-State Circuits. 43(2): 566–576. Bibcode:2008IJSSC..43..566L. doi:10.1109/JSSC.2007.914337. ISSN 0018-9200. S2CID 6119048.

[16] C. Posch; D. Matolin; R. Wohlgenannt, (January 2011). "A QVGA 143 dB Dynamic Range Frame-Free PWM Image Sensor With Lossless Pixel-Level Video Compression and Time-Domain CDS". IEEE Journal of Solid-State Circuits. 46 (1): 259–275. Bibcode:2011IJSSC..46..259P. doi:10.1109/JSSC.2010.2085952. ISSN 0018-9200. S2CID 21317717.

[17] A. Nicholas; J. Wolf; L. Kordella; C. Brown; T. Finne; S. Budzien; K. Marr; C. Englert, "On-orbit Optical Detection of Lethal Non-Trackable Debris." Proceedings of the 73rd International Astronautical Congress, A6.1.71592, Paris France, (2022).